Tullio Marta (Orcid ID: 0000-0001-8834-9706)

RESEARCH ARTICLE - APPLICATION

Computational fluid dynamics of the airways after left-upper pulmonary lobectomy: a case study

Marta Tullio[1*], Lorenzo Aliboni[1*], Francesca Pennati[1], Rosaria Carrinola[3], Alessandro Palleschi[2,3], Andrea Aliverti[1]

[1] Dipartimento di Elettronica, Informazione e Bioingegneria, Politecnico di Milano, Italy

[2] University of Milan, Department of Pathophysiology and Transplantation, Milan, Italy

[3] Thoracic Surgery and Lung Transplantation Unit, Fondazione IRCCS Ca' Granda Ospedale Maggiore Policlinico of Milan, Italy

[*]MT and LA equally contributed to this manuscript.

Abstract

Pulmonary lobectomy is the gold standard intervention for lung cancer removal and consists in the complete resection of the affected lung lobe, which, coupled with the re-adaptation of the remaining thoracic structures, decreases the postoperative pulmonary function of the patient. Current clinical practice, based on spirometry and cardiopulmonary exercise tests, does not consider local changes, providing an average at-the-mouth estimation of residual functionality. Computational Fluid Dynamics (CFD) has proved a valuable solution to obtain quantitative and local information about airways airflow dynamics.

A CFD investigation was performed on the airway tree of a left-upper pulmonary lobectomy patient, to quantify the effects of the postoperative alterations. The patient-specific bronchial models were reconstructed from pre- and postoperative CT scans. A parametric laryngeal model was merged to the geometries to account for physiological-like inlet conditions. Numerical simulations were performed in Fluent®.

This article has been accepted for publication and undergone full peer review but has not been through the copyediting, typesetting, pagination and proofreading process which may lead to differences between this version and the Version of Record. Please cite this article as doi: 10.1002/cnm.3462

The postoperative configuration revealed fluid dynamic variations in terms of global velocity (+23%), wall pressure (+48%), and wall shear stress (+39%). Local flow disturbances emerged at the resection site: a high-velocity peak of 4.92 m/s was found at the left-lower lobe entrance, with a local increase of pressure at the suture zone (18 Pa). The magnitude of pressure and secondary flows increased in the trachea and flow dynamics variations were observed also in the contralateral lung, causing altered lobar ventilation.

The results confirmed that CFD is a patient-specific approach for a quantitative evaluation of fluid dynamics parameters and local ventilation proving additional information with respect to current clinical approaches.

KEYWORDS

computational fluid dynamics, pulmonary lobectomy, imaged-based, tracheobronchial tree modeling

Correspondence

Marta Tullio,

TBMLab - Laboratorio di Tecnologie Biomediche,

Dipartimento di Elettronica, Informazione e Bioingegneria (DEIB),

Politecnico di Milano

Via Colombo, 40 (2° floor), 20133 Milan, Italy.

E-mail: marta.tullio@polimi.it

1. Introduction

Pulmonary lobectomy is the most common surgical intervention for lung cancer removal and consists in the total excision of an entire lung lobe. It is the only curative and unpreventable treatment for patients with localized lung tumor. Postoperative consequences include structural modifications in the thoracic space: the hemithoracic volume on the side of surgery decreases, the hemidiaphragm rises upward, and the mediastinum shifts towards the lobectomy side [1,2]. Such displacements determine deformity of the residual structures, which could lead to bronchial kinking and/or obstruction of the airways in severe cases [2–5]. These alterations could further reduce pulmonary function, which is already compromised by the permanent loss of respiratory tissue and by possible existing comorbidities.

Compensatory overinflation in the remaining lobes could help to balance the loss of air volume: alveolar tissue regrowth, structural remodeling, and progressive functional compensation in the long-term after surgery are proven [6,7]. Differences are reported among lower, middle, and upper lobectomy postoperative changes [3,8,9].

The prediction of postoperative pulmonary function is crucial for establishing surgical risk before the operation, but the current clinical practice relies only on preoperative pulmonary function tests (i.e. spirometry and cardiopulmonary exercise tests) [10]. Nevertheless, these methods do not consider volume differences among pulmonary segments and lobes, tissue heterogeneity, and postoperative alterations of lung and airways anatomy [11,12]. Moreover, the follow-up techniques for monitoring the patient after surgery do not allow local non-invasive inspection of the airways. Therefore, further investigations on the impact of lobectomy are needed.

Computational Fluid Dynamics (CFD) represents an attractive tool to overcome the drawbacks of the current clinical approaches, providing quantitative information on regional ventilation, lobar flow rate, and local properties at every location in the airways [8,13–15]. The geometrical model of the airways can be reconstructed from the CT-images of the patient [14–21], allowing to replicate the anatomical peculiarities of a subject and to study the effects of lung pathologies. Burrowes et al.

modeled the morphological changes due to asthma and chronic obstructive pulmonary disease (COPD) [22,23], while De Backer et al. showed the fluid dynamic consequences of such pathologies [14,21]. Bos et al. simulated the deposition of antibiotics in the airways of cystic fibrosis patients [19]. Qi et al. studied the air flow dynamics in case of congenital anomalies like tracheal bronchus and left pulmonary artery sling [20,24]. The fluid dynamics effects of pulmonary lobectomy were also studied by Gu et al. [8], who performed CFD simulations on the airway tree of 18 left-upper-lobectomy patients.

Usually, most of the clinical CT scan protocols image only the thoracic tract of the respiratory system to limit the x-ray exposure of the patient's head. Therefore, the geometrical reconstructions from the images are generally limited to the tracheobronchial tree, deprived of the upper airways.

Lin et al. [25] studied the effects of the upper airways on the downstream flow. The complete CT-based geometry was compared to the truncated tracheobronchial tree: the fluid flow structures turned out to be strongly different in the two cases. In the complete model, a high-speed laryngeal jet formed with the flow passage through the glottis, determining turbulent features and flow rotational motions in the trachea. On the contrary, the truncated model presented a parabolic velocity profile, typical of laminar flows. The comparison of flow characteristics in the two models demonstrated that simple inlet boundary conditions do not adequately represent the effects of the upper airways, affecting flow properties through several generations. Choi et al. [17] deepened the issue by comparing different levels of truncation of the upper airways, demonstrating that the main responsible structure for turbulence in the lower airways is the glottal restriction. However, the inclusion of the extra-thoracic airways in the CT-imaging is an uncommon occurrence. Thus, other authors proposed different models to replicate the effects of the upper structures in the fluid flow [15,26–29].

Some authors applied patient-specific boundary conditions elaborating CT-image sets recorded at different lung volumes [14,26,30]. However, the acquisition of more than one CT-image set for the same subject is unusual, and the greatest part of authors in literature apply uniform and steady boundary conditions at the outlets [8,15,17,20,25,28,31].

In the present work, a numerical investigation was performed on one patient, who underwent a left-upper pulmonary lobectomy intervention, to evaluate the postsurgical alterations effects in the airflow dynamics.

The specific aims were the following: a) simulate the laryngeal jet effects by introducing the artificial model of the larynx proposed by Miyawaki at al. [26], merged at the superior portion of the trachea; b) provide a description of specific fluid dynamics parameters (velocity, pressure, wall-shear stress), in presence of an accurate geometry reconstruction, both in the whole airway tree and in the site of surgery.

2. Materials and Methods

2.1. Study design

The study involved a 70-years old female patient, who underwent left-upper lobectomy for squamous cells carcinoma, through video-assisted thoracoscopic surgery (VATS). Chest CT images, acquired in breath-hold at full-inspiration before and after surgery, were retrospectively collected. The patient provided written informed consent for using the data for research purposes. All identifying information was removed from the CT images before the analysis. The CT acquisition parameters are summarized in Table 1.

2.2. Generation of the airway model

The 3D subject-specific models of the airway tree were segmented from the CT images of the preoperative and postoperative configurations (Figure 1). First, an automatic segmentation algorithm based on 3D confidence-connected region growing (CCRG) [32], developed in C++, was applied. Second, the manual dynamic region-growing segmentation was carried out to complete the geometry reconstruction in Mimics (Materialise NV, Belgium).

The geometrical reconstructions were processed with 3-Matic (Materialise NV, Belgium) and ANSYS SpaceClaim.

To reproduce the turbulent airflow features in the trachea, the laryngeal jet model developed by Miyawaki et al [26] was recreated and merged to the geometries (Figure 2). The dimensions of this model, shaped as a convergent/divergent pipe, were obtained from a large set of data recorded at end-inspiration, with the glottis in the fully opened configuration [26]. Five fundamental lengths were provided as a function of the hydraulic diameter of the trachea $D_{h,t}$: the hydraulic diameter at the glottis $D_{h,g}=0.677D_{h,t}$; the hydraulic diameter upstream the glottis $D_{h,gu}=1.24D_{h,t}$; the length of the larynx upstream the glottis $l_{gu}=1.3D_{h,t}$; the length of the larynx downstream the glottis $l_{gl}=1.3D_{h,t}$; and the length of the trachea from the glottis to the carina $L_g=8.64D_{h,t}$ (not shown in figure). The

values obtained for the corresponding models in the preoperative and in the postoperative case are summarized in Table 2.

The application of such model was meant to simulate a physiological-like boundary condition at the inlet of the airway tree, replicating the effects of the glottal restriction, which was not included in the CT-images. The final geometrical domains for numerical simulations are shown in Figure 3.

2.3. CFD Mesh generation

A tetrahedral unstructured grid type was chosen due to the geometrical complexity. To correctly resolve fluid flow properties in the sub-viscous layer proximal to the wall, 15 inflation layers were created. The first layer thickness was set equal to 0.01 mm, which correspond to an estimated $y^+ < 1$. The quality of the generated mesh was evaluated through the maximum skewness criterion (equilateral volume skewness < 0.90).

Three mesh refinements were automatically generated for each geometry in Fluent®, with a total number of cells of 10.0×10^6, 12.5×10^6, and 23.0×10^6 for the preoperative case, and 6.5×10^6, 9.0×10^6, and 18.9×10^6 for the postoperative case. Mesh parameters, including the maximum size of bulk cells and the maximum skewness, are reported in Table 3.

The convergence analysis was conducted considering the relative variations between the meshes in terms of volume flow rate (VFR) at the outlets, with a tolerance inferior to 0.5%. Moreover, the local velocity profile was evaluated for the three meshes at a cross-sectional plane at 2 cm distance from the carina. Three axes, mutually rotated at 60° from each other, were chosen to plot the profiles (Figure 4). The three meshes did not show significant differences in the velocity profile in both cases.

2.4. Airflow simulation

Given the dynamic nature of breathing, the influence of oscillatory behavior on the flow was preliminarily investigated. As previously demonstrated, the importance of unsteadiness on the average flow characteristics, obtained through a steady solution, is modest if the Womersley number (Wo) is less than 10 and the Strouhal number is less than 1 [33]. The Womersley number, i.e., the ratio of unsteady forces to viscous forces, is calculated as:

$$Wo = \frac{D_{h,t}}{2}\left(\frac{2\pi f}{\nu}\right)^{0.5} \quad (2.1)$$

The Strouhal number (S), i.e., the ratio of unsteady forces to inertial forces, is calculated as:

$$S = \frac{2\pi f D_{h,t}}{\bar{u}} \quad (2.2)$$

Where f is the breathing frequency, υ is the air kinematic viscosity, $D_{h,t}$ is the hydraulic diameter of the trachea, and $\bar{u}$ is the average velocity at the corresponding diameter.

In the case under analysis, f=15 breaths per minute and υ=1.79×10^{-5} kg/ms, $D_{h.t}$, measured from the model inlet cross-section, was 1.66 cm and 1.57 cm in the preoperative and postoperative geometry, respectively. Therefore, in the preoperative case, Wo=2.45 and S=0.017, whereas in the postoperative case, Wo=2.33 and S=0.015. Consequently, a static analysis was performed, considering an averaged tidal breathing flow rate of 0.5 L/s.

CFD simulations were performed by using the finite volumes method (FVM) for the numerical solution of the mass conservation and the Navier-Stokes equations in the 3D domain. The effects of turbulence were modeled using the Shear Stress Transport (SST) k-ω model with Low Reynolds Number (LRN) correction, which is considered the most suitable model for predicting low turbulence flow in the respiratory system, with the available computational resources [8,15,33–35].

A steady inspiratory velocity was set as boundary condition at the larynx inlet. The inlet velocity was calculated for each geometry as the volume flow rate divided by the inlet cross-sectional area. A value of 1.5 m/s was obtained for the preoperative case, and a value of 1.7 m/s for the postoperative case. A turbulent intensity of 5% and a viscosity ratio μ_T /μ of 10 were applied. A uniform reference pressure was set at each outlet boundary, corresponding to the cross-sectional surface at the terminal end of each bronchus. A no-slip condition was imposed at the walls, considered rigid, stationary, and smooth. The air was considered as an incompressible Newtonian fluid, with density ρ equal to 1.225 kg/m^3 and dynamic viscosity μ equal to 1.79×10^{-5} kg/ms. This is an acceptable assumption for the airflow in the human airways, where the Mac number is close to 0.3, and the effects of temperature and humidity cause negligible variations on the air properties with respect to environmental conditions [33,36].

The hypothesis of rigid walls with no-slip condition is well documented in literature [16,26,27,33,37]. This can be considered reasonably valid due to the relatively high percentage of cartilage in the airway tissue up of the central airways [38].

The following numerical methods were chosen: pressure-based solver; second-order upwind scheme for the momentum equations; Green-Gauss cell-based method for gradients evaluation, and SIMPLE algorithm for pressure-velocity coupling. Convergence was set as residuals less than 10^{-6}. Calculations were stopped when the residuals converged, and the solution was evaluated to be stable.

The results were reported in terms of velocity magnitude, wall pressure and wall shear stress, in the entire tree, with a global and a local point of view. Also, velocity components at specific cross-sectional planes were reported. The first plane was positioned at the inlet of the trachea, just downstream the laryngeal model. The second plane was located at a 2 cm distance from the carina. The remaining cross-sectional planes were positioned at the half of the following branches: on the right-hand side, the right main bronchus, bifurcating into the right upper bronchus and the intermediate bronchus, bifurcating into the right middle lateral, the right middle medial, and the right

lower bronchi; on the left-hand side, the left main bronchus, bifurcating into left upper bronchus (which was missing in the postoperative geometry) and left lower bronchus. Thus, a total of 11 planes were considered for the preoperative geometry, and a total of 10 planes for the postoperative geometry.

The regional ventilation was obtained for both cases to reveal the contribution of each lung portion to the pulmonary functionality and highlight how it changed after lobectomy.

3. Results

Overall, the postoperative configuration showed an increment in the magnitude of velocity, pressure, and wall shear stress, with the same inlet flow rate as the preoperative case. Peak values of the variables of interest are reported in Table 4. The maximum value of velocity, located at the inlet of the tree, was 4.16 m/s in the preoperative configuration and 5.40 m/s in the postoperative one. The peak value of pressure and wall shear stress, located at the carina bifurcation, was almost doubled in the postoperative case: a maximum pressure of 11.87 Pa and 22.96 Pa, and a maximum wall shear stress of 1.03 Pa and 1.69 Pa, were found for the preoperative and postoperative case, respectively.

The velocity streamlines, the wall pressure, and the wall shear stress are shown in Figure 5 for the preoperative and postoperative cases. Air dynamic conditions worsened in the whole postoperative tree, with greater velocity values propagating up to the smallest branching generations (Figures 5a and 5b). Consequently, wider regions of high wall shear stress, corresponding to the areas of high-velocity gradients, were observed (Figures 5e and 5f). The entire postoperative tree was subjected to higher pressure (Figures 5c and 5d). The pressure settled down in the vicinity of the outlets in both geometries, where the uniform boundary condition was applied.

Interestingly, consequences of the lobectomy were also observable on the right side of the tree, where no surgical intervention was performed, probably due to the increased regional flow rate in the non-

resected lung. Higher velocity, pressure, and wall shear stress values were found with respect to the preoperative right side, especially in the lower part. The average velocity at the entrance of the intermediate right bronchus increased from 1.66 m/s to 1.74 m/s. The average wall pressure increased from 3.99 Pa to 10.85 Pa, with peak values at the bifurcations increasing from 8.85 Pa to 19.77 Pa. The maximum value of wall shear stress increased as well from 1.03 Pa to 1.27 Pa at the bifurcations.

In Figure 6, the fluid dynamics comparison between the preoperative and postoperative trachea is shown. In the preoperative situation, smoother gradients of velocity, and more uniform pressure and wall shear stress values were present. After surgery, the trachea assumed a deformed configuration, characterized by severe curvatures. Higher velocity peaks of about 4.8 m/s were found at the inner part of the curvatures (Figure 6b), while important higher-pressure zones were found at the curvatures outer part and at the carina bifurcation, with peak values in the range of 18.07 – 22.96 Pa (Figure 6d). Regions of high wall shear stress became wider in the postoperative trachea and at the carina (Figure 6f).

In Figure 7, the fluid dynamics comparison is focused on the site of surgery. Before the lobectomy, the airflow divided among the upper and lower left bronchi with smooth velocity gradients (Figure 7a). After surgery, this zone presented severe distortions as well: the left main bronchus was twisted upward, and the left-lower bronchus severely bent just downstream the suture zone, shrinking its lumen. The air entered the left lower lobe with a higher speed with respect to the preoperative case, with a peak value equal to 4.92 m/s (Figure 7b). This can be explained considering both the lack of the left-upper bronchus and the restriction of the bronchus lumen, which caused a larger flow rate to pass through a narrower cross-section. In the suture zone and in the following bifurcations, a peak of pressure in the range of 16-18 Pa was found. Considerably lower pressure occurred in the same zone for the preoperative case, in the range of 5-7 Pa and about 10 Pa at the bifurcations (Figures 7c and 7d). In the postoperative situation, higher wall shear stress values up to 1.6 Pa were found, which did not occur in the preoperative bifurcations at the same generation level (0.6 Pa).

However, for both cases, the peak values of wall shear stress were located at the bifurcations, where the velocity gradients were steeper (Figure 7e and 7f). This result is coherent with other studies in literature [15,39].

Axial velocity profiles, of normal direction with respect to the cross-sectional planes, are shown in Figure 8. In the upper part of the trachea, the peak velocity, of magnitude equal to 5.4 m/s, was shifted towards the inner part of the tracheal curvature, with a small peak of reverse flow (0.5 m/s) at the opposite side. Reverse flow was also found at the carina level, which showed a quite irregular profile in the postoperative case. This result is in accordance with Luo et al. [15], who performed a LRN k-ω simulation including the glottal restriction.

In the airways downstream the following bifurcations, axial velocity profiles showed a skewed peak towards the inner part of the conduits, as reported by other authors [15,24,25,39,40], with greater values in all the postoperative planes, especially at the trachea and at the left bronchus restriction. A strong variation was found at the entrance of the left-lower bronchus: the axial velocity increased from 2.5 m/s before surgery to 4.5 m/s after surgery.

Axial velocity contours with in-plane velocity components are shown in Figure 9 for the preoperative (a) and postoperative (b) cases. The axial velocity ranged from -0.50 m/s to 5.40 m/s, while the maximum value of tangential velocity was 2.04 m/s. In general, the in-plane velocity always presented a rotational pattern in both cases, with higher magnitude values in the whole tree after surgery. It was demonstrated that flows in curved ducts exhibit a local imbalance between inertial (centrifugal) forces and pressure gradients, which causes the velocity peak to shift from the center of the section and secondary circulations [41]. A similar phenomenon occurred in the curve-shaped postoperative trachea: at the inlet of the trachea, the axial velocity peak was shifted to the inner side of the curvature, as can be observed both in Figure 8 and 9, and the tangential velocity vectors demonstrated the presence of secondary circulation, as can be observed in Figure 9. These results are

coherent with other findings in literature: Lin et al. [25], who performed a Direct Numerical Simulation (DNS) to study the effects of the laryngeal jet on the downstream flow, found rotational motions at the level of the trachea.

Close to the carina, the velocity was disturbed as well after surgery, with increased magnitude and intensified rotational pattern of tangential vectors. A similar behavior was found in all the other plates, except for the left main bronchus plate, where the postoperative rotational component diminished. As previously mentioned, at the right side of the tree, the intermediate bronchus plate presented increased values of velocity components.

The strong variation on the left side of the tree after surgery is clearly visible in the plates of Figure 9: the left-upper bronchus was missing in the postoperative configuration and the left-lower bronchus presented a significant reduction in the cross-sectional area. Here, the magnitude of the tangential vectors increased significantly and was comparable to the trachea conditions. The axial vectors increased too, in accordance with previous observations.

In Figure 10, the regional VFR is reported in percentage values for the following regions: right-upper lobe (RUL), right-middle lobe (RML), right-lower lobe (RLL), left-upper lobe (LUL), left-lower lobe (LLL), right lung (RL) and left lung (LL).

The regional VFR demonstrated a greater ventilation in the right lung with respect to the left lung. This was an expected result because the right lung presents a greater volume [33,42,43]. The lower lobes (RLL, LLL) received the greater portion of inhaled flow rate with respect to the upper lobes (RUL, LUL). The right middle lobe (RML), which is the smallest lung lobe, received the lowest amount of flow rate. Airflow dynamics and particle deposition studies also confirmed these findings [15,28,44]. After pulmonary lobectomy, the different ventilation among the two lungs became more pronounced: the regional VFR in the RL increased from 55.1% to 64.6%, while in the LL diminished from 44.9% to 35.4%. Locally, after lung resection, the RUL ventilation was almost unchanged, while an increased VFR was present in RML and in the RLL. A null VFR occurred at the LUL due to the

missing lobe, and a remarkable ventilation increment occurred at the LLL, from 22.8% to 35.4%. Analogous study in literature also predicted a comparable redistribution of regional ventilation towards the contralateral side after surgery [8]. Clinical studies on pulmonary function after lobectomy evidenced a reduction in volume variation on the side of surgery [45,46].

The regional pressure drops across the lobar bronchi were calculated and reported in Table 5. The pressure at the entrance of each lobe was obtained as the average value in the cross-sectional area. The reference cross-sections were indicated in Figure 8 for the RUL, the medial and lateral RML, the RLL, the LUL and the LLL. Each regional pressure drop was calculated with respect to the outlet reference pressure. Before surgery, the pressure drops across the lobes ranged from 4.5 to 6.28 Pa, while after surgery values ranging from 13.41 to 16.36 Pa were reached. The postoperative pressure drops increased with an almost uniform increment ranging from 8.76 to 10.39 Pa, with the greatest values for the RUL and the LLL. This was an expected result, considering the wall pressure contours shown in Figure 5, where a comparable increment was verified in the whole postoperative geometry upstream the suture zone.

4 Discussion

In the present work, a CFD method was proposed to study the postoperative fluid dynamics following a left-upper pulmonary lobectomy, reconstructing a patient specific geometry from CT images before and after surgery, and providing a physiological-like inlet boundary condition.

The laryngeal jet caused by the glottal constriction is an important factor to be considered, conferring turbulence features to the airflow [17,25,26]. The use of the laryngeal model based on Miyawaki et al. [26] represented a valid and feasible alternative to the missing superior airways in the CT images: the cross-sectional restriction of the model provided a local acceleration of the airflow, which replicated the fluid dynamics effects of the glottis. Moreover, involving normalized parametric

dimensions with respect to the trachea hydraulic diameter, it was tailored to the airway trees proportionally to the anatomical dimensions.

The airflow simulations were performed according to the previously reported approach, in lack of directly measured data from the patient, CT-imaging of the complete upper airways, and having only one image-set at a specific volume available [8,17,24,25,27,31]. With respect to Lin et al. and Choi et al. [17,25], who imposed a fixed outflow, the condition of uniform pressure was set at the outlet boundaries, to not constrain the airflow partition and the lobar flow rates [15]. The mesh independence analysis was performed, obtaining improved mesh refinements with respect to analogous studies in literature [8].

Comparing the two situations, with the same inlet flow rate, increased mechanical stimuli emerged in the postoperative structure. Our results showed increased velocity, pressure, and wall shear stress values in the whole airway tree after pulmonary lobectomy, deriving not only from the resection of an entire lung lobe, but also from the geometrical adaptation of the remaining structures (Figures 5, 6 and 7). Also, the turbulent characteristics of the airflow, related to the tangential component of the velocity, have shown a worsening (Figure 9).

The regional pressure drops reported in Table 5 demonstrated an almost uniform pressure increment in all the lobar bronchi after surgery, confirming once again that lobectomy consequences affected the whole structure. In particular, local results at the resection site (Figure 7) suggested that the sudden narrowing of bronchial lumen just downstream the suture might have caused a high fluid dynamic resistance to airflow and a consequent driven pressure increase during inspiration [20,47,48]. The bronchial stenosis, together with the severe bending of the left-lower bronchus, might have impaired air passage, worsening fluid dynamic conditions at the bifurcations of the left side of the tree. The higher wall shear stress values, determined by the increase of local velocity in this region represent a potential risk for endothelial cells of the bronchial tissue [40], especially if higher inlet flow rates occur, such as in the case of exercise conditions.

The geometrical displacements and deformations are an inevitable consequence of lobar excision, and normally involve all the surrounding organs of the thoracic space, including the trachea and the larger bronchi [49,50]. However, very little literature exists on quantitative morphological characterization, field of research in which further studies are required. The effect of standard respiratory physiotherapy on long term postoperative complications after lung resection is still an investigation subject, and the role of each structural modification on postoperative pulmonary function is not entirely clear [51].

As already mentioned, regional ventilation globally redistributes to the contralateral side after lobectomy, and the remaining lobes receive a greater flow rate as compensatory response. Clinical studies reported a decrease in spirometry parameters (FVC and FEV1) after lobectomy, indicating an overall reduction of pulmonary function [5,7,46,52]. However, poor literature exists about local alteration of pulmonary function and fluid dynamics consequences. A recent clinical study on postoperative patients demonstrated the difficulty in measuring lobar ventilation redistribution through functional imaging (especially for surgery on the left side), due to the mediastinum shifting and geometry readaptation [45]. Therefore, the computational approach adopted in the present study may help in revealing local fluid dynamics parameters and in determining lobar ventilation (Figure 10).

Performing a CFD simulation on the anatomy of a particular patient, and analyzing the fluid dynamic parameters that will emerge, could allow the prescription of a personalized respiratory physiotherapy for a better postoperative management. In addition, the present study highlights the need for a more exhaustive research on lobectomy consequences, in order to assess pre- and post-operative functionality in relation to the structural modifications and to the resected lobe.

4.1. Limitations and future developments

The present work is affected by different limitations deriving from some missing input data and the computational resources at disposal.

A more complete patient-specific CFD simulation should involve the setting of appropriate boundary conditions, elaborating CT images at different lung volumes to derive the specific lobar flow rate of the patient [14,26,30,53]. Unfortunately, the standard clinical practice does not provide the acquisition of more than one CT-image set for lobectomy patient care. Therefore, as the greatest part of authors in literature, a uniform pressure at the outlets was applied in the present work. For a better fluid dynamics evaluation of the patient breathing conditions, the CT recording of, at least, two different lung volumes would be preferable to estimate a more realistic lobar ventilation. Also, a future development could be the validation of the numerical solution through reliable measured data derived, for example, from functional imaging techniques [14,15,21].

A more comprehensive study could be obtained involving more pulmonary lobectomy patients. The postoperative consequences may change depending on the resected lobe and on the anatomical characteristics of the subject. Therefore, patients undergoing different kind of surgery should be evaluated in a sufficient number, so to obtain a statistically affordable study. A morphometric evaluation of the geometrical adaptation due to surgery could be performed to characterize each kind of pulmonary lobectomy.

In the present study, a static inspiratory flow rate was analyzed. The choice of the inspiration condition is related to the fact that it is the respiratory phase generally analyzed during preoperative evaluation and postoperative follow up for oncological patients. Moreover, higher mechanical stimuli occur in the airway walls, with respect to the expiratory condition [54,55]. A relevant outcome is the situation at the resection site shown in the results, where higher wall pressure and wall shear stresses emerged at the suture and at the bifurcations (Figure 6). To further complete the analysis, it would be of interest to study the expiratory condition as well. However, in a computational context, this results

in a high degree of approximation: to provide an inlet condition for exhalation, hypothesis on the fluid dynamic conditions at each bronchial ending, or on lobar ventilation should be assumed, in lack of a second CT-image set, or functional imaging data.

A more realistic simulation should involve a dynamic inlet flow rate, adopting a physiological-like breathing waveform [31,54]. However, the static assumption is a reasonable simplification considering the Womersley number and the Strouhal number for the problem of interest. Therefore, similar outcomes could be expected by performing a dynamic simulation. The present analysis was performed at the same tidal breathing conditions among pre- and postoperative situations. A recent study measured the thoraco-abdominal volume variation in a cohort of lobectomy patients through opto-electronic plethysmography, comparing two surgery kind: open thoracotomy and VATS [46]. During quite breathing, it was shown that the minute ventilation, which is a measure of the breathing flow, did not undergo changes after lung resection with respect to the preoperative one. A slight variation occurred in respiratory rate and tidal volume in case of open thoracotomy, but, interestingly, in VATS patients these differences were almost imperceptible. Since relevant differences in minute ventilation were not reported, and since the patient in our study was subjected to VATS lobectomy, the same volume flow rate was reasonably imposed as inlet condition for the preoperative and postoperative models in the present study. To better understand the real conditions of the patient, the volume variation with respect to time, registered before and after surgery, could be applied as input variable for the models. The investigation should be further deepened considering different breathing conditions, as happens during exercise or mechanical ventilation, including the real breathing wave form of the patients or flow rate data from literature [46].

To date, a complete reconstruction of the airway tree cannot be achieved due to the intrinsic limitations of the CT-imaging resolution and the segmentation techniques. Despite this, particular attention was given to the extraction of all the visible bronchi in their entire length and cross-sectional dimensions. Some authors, like Tawhai and co-workers completed the airway tree by using a volume-

filling algorithm to generate airway centerline locations within lungs volume [53,56]. Nonetheless, a good compromise must be found between numerical method feasibility and geometry complexity [54].

Although most of the approaches presented in literature do not comprise or model the effects of the superior airways, their presence would be preferable to replicate physiologic conditions in CFD simulations. A solution to the simplified model adopted in this study could be the application of more realistic models [27,28], or better, the acquisition of the patient upper airways in clinical CT scan protocols.

The hypothesis of rigid walls, although being acceptable for the central airways, is less appropriate for the peripheral airways, where the cartilage content diminishes. Unfortunately, fluid-structure interaction computation is prohibitive for an extended airway tree model, considering also the anisotropic and hyperelastic nature of the tissue [57]. Moreover, in this study, a static analysis at a specific inspiratory lung volume was conducted, justifying the choice of not modeling the inflation/deflation behavior during breathing.

The effects of temperature and humidity on air properties were not modeled in this work, despite changes in density and viscosity can occur passing through the upper airways. These effects should be included in the numerical model to perform a more detailed analysis.

A turbulence model was adopted to predict the solution, implicitly admitting the fluid flow to be statistically stationary in its average properties. The process of breathing, however, presents an oscillatory behavior and regions of different fluid dynamic conditions: turbulent in larger airways, transitional, and laminar in the peripheral segments. This could lead to uncertainty in the solution at local level. The choice of using a Reynolds-Averaged Navier Stokes (RANS) model was determined by the computational resources. However, the SST k-ω model was adopted by many authors, demonstrating to be affordable in predicting the flow properties in the respiratory system, although its model constants were not originally determined for the fluid flow inside the airways

[8,15,24,33,35,58]. A previous study successfully demonstrated the appropriateness of the model in predicting average quantities, by comparing it with DNS results in normal airways [55]. The present study evidenced turbulence instabilities in the larger airways, due to the laryngeal model [15,17,25,26], and to geometrical distortions, especially after surgery. These considerations demonstrated that the adopted SST k-ω model with LRN correction can predict fluid behavior in the airway tree, at least in an average sense. Despite this, a future investigation using LES or DNS should be performed to ensure the accuracy of the RANS model in presence of pronounced deformations of the airways [59].

5. Conclusions

A CFD methodology to study the consequences of anatomical post-surgery alterations on airflow dynamics, in a patient-specific airway tree model, was proposed.

The effects of the laryngeal jet, which is responsible of flow characteristics in the trachea, were reproduced, providing a physiological-like inlet condition to the model.

The airflow disturbances derived not only from the resection of an entire lung lobe, but also from the geometrical adaptation of the remaining structures, were quantified. Turbulent instabilities increased in the highly distorted postoperative configuration. Higher maximum values were found in pressure, wall shear stress, axial and tangential velocity, even if an averaged tidal flow rate was simulated. The local results showed a dramatic restriction of the bronchial cross-section in the site of surgery, where worsening fluid dynamics conditions were found. The trachea of the patient was also subjected to surgery outcomes, indicating that possible complications could indirectly affect other regions.

ACKNOWLEGMENT

We thank PARAMETRIC DESIGN SRL for computational resources and technical consulting.

CONFLICT OF INTEREST

All the authors declare no conflicts of interest.

DATA ACCESSIBILITY

The data that support the findings of this study are available on request from the corresponding author. The data are not publicly available due to privacy or ethical restrictions.

REFERENCES

1. Kang YR, Kim JS, Cha YK, Jeong YJ. Imaging findings of complications after thoracic surgery. *Japanese Journal of Radiology* 2019; **37**(3):209–219. doi:10.1007/s11604-018-00806-y.

2. Alpert JB, Godoy MCB, deGroot PM, Truong MT, Ko JP. Imaging the Post-Thoracotomy Patient. Anatomic Changes and Postoperative Complications. *Radiologic Clinics of North America* 2014; **52**(1):85–103. doi:10.1016/j.rcl.2013.08.008.

3. Kim SJ, Lee YJ, Park JS, et al. Changes in pulmonary function in lung cancer patients after video-assisted thoracic surgery. *Annals of Thoracic Surgery* 2015; **99**(1):210–217. doi:10.1016/j.athoracsur.2014.07.066.

4. Seok Y, Cho S, Lee JY, Yang HC, Kim K, Jheon S. The effect of postoperative change in bronchial angle on postoperative pulmonary function after upper lobectomy in lung cancer patients. *Interactive Cardiovascular and Thoracic Surgery* 2014; **18**(2):183–189. doi:10.1093/icvts/ivt463.

5. Ueda K, Tanaka T, Hayashi M, Tanaka N, Li TS, Hamano K. Clinical ramifications of bronchial kink after upper lobectomy. *Annals of Thoracic Surgery* 2012; **93**(1):259–265. doi:10.1016/j.athoracsur.2011.08.065.

6. Toney LK, Wanner M, Miyaoka RS, Alessio AM, Wood DE, Vesselle H. Improved prediction of lobar perfusion contribution using technetium-99m-labeled macroaggregate of albumin single photon emission computed tomography/computed tomography with attenuation correction. *Journal of Thoracic and Cardiovascular Surgery* 2014; **148**(5):2345–2352. doi:10.1016/j.jtcvs.2014.04.036.

7. Ueda K, Tanaka T, Hayashi M, et al. Compensation of pulmonary function after upper lobectomy versus lower lobectomy. *Journal of Thoracic and Cardiovascular Surgery* 2011; **142**(4):762–767. doi:10.1016/j.jtcvs.2011.04.037.

8. Gu Q, Qi S, Yue Y, et al. Structural and functional alterations of the tracheobronchial tree after left upper pulmonary lobectomy for lung cancer. *BioMedical Engineering Online* 2019; **18**(1):1–18. doi:10.1186/s12938-019-0722-6.

9. Sengul AT, Sahin B, Celenk C, Basoglu A. Postoperative lung volume change depending on the resected lobe. *Thoracic and Cardiovascular Surgeon* 2013; **61**(2):131–137. doi:10.1055/s-0032-1322625.

10. Brunelli A, Charloux A, Bolliger CT, et al. ERS/ESTS clinical guidelines on fitness for radical therapy in lung cancer patients (surgery and chemo-radiotherapy). *European Respiratory Journal* 2009; **34**(1):17–41. doi:10.1183/09031936.00184308.

11. Miserocchi G, Beretta E, Rivolta I. Respiratory Mechanics and Fluid Dynamics After Lung Resection Surgery. *Thoracic Surgery Clinics* 2010; **20**(3):345–357. doi:10.1016/j.thorsurg.2010.03.001.

12. Licker MJ, Widikker I, Robert J, et al. Operative Mortality and Respiratory Complications After Lung Resection for Cancer: Impact of Chronic Obstructive Pulmonary Disease and Time Trends. *Annals of Thoracic Surgery* 2006; **81**(5):1830–1837. doi:10.1016/j.athoracsur.2005.11.048.

13. Burrowes KS, De Backer J, Kumar H. Image-based computational fluid dynamics in the lung: virtual reality or new clinical practice? *Wiley Interdisciplinary Reviews: Systems Biology and Medicine* 2017; **9**(6):1–16. doi:10.1002/wsbm.1392.

14. De Backer JW, Vos WG, Gorlé CD, et al. Flow analyses in the lower airways: Patient-specific model and boundary conditions. *Medical Engineering and Physics* 2008; **30**(7):872–879. doi:10.1016/j.medengphy.2007.11.002.

15. Luo HY, Liu Y. Modeling the bifurcating flow in a CT-scanned human lung airway. *Journal of Biomechanics* 2008; **41**(12):2681–2688. doi:10.1016/j.jbiomech.2008.06.018.

16. Oakes JM, Roth SC, Shadden SC. Airflow Simulations in Infant, Child, and Adult Pulmonary Conducting Airways. *Annals of Biomedical Engineering* 2018; **46**(3):498–512. doi:10.1007/s10439-017-1971-9.

17. Choi J, Tawhai MH, Hoffman EA, Lin CL. On intra- and intersubject variabilities of airflow in the human lungs. *Physics of Fluids* 2009; **21**(10):1–17. doi:10.1063/1.3247170.

18. Yin Y, Choi J, Hoffman EA, Tawhai MH, Lin C-L. Simulation of pulmonary air flow with a subject-

specific boundary condition. *Journal of Biomechanics* 2010; **43**(11):2159–2163. doi:10.1016/j.jbiomech.2010.03.048.

19. Bos AC, Van Holsbeke C, De Backer JW, et al. Patient-specific modeling of regional antibiotic concentration levels in airways of patients with cystic fibrosis: Are we dosing high enough? *PLoS ONE* 2015; **10**(3):1–20. doi:10.1371/journal.pone.0118454.

20. Qi S, Li Z, Yue Y, van Triest HJW, Kang Y. Computational fluid dynamics simulation of airflow in the trachea and main bronchi for the subjects with left pulmonary artery sling. *BioMedical Engineering Online* 2014; **13**(1):1–15. doi:10.1186/1475-925X-13-85.

21. Vos W, Backer JW De, Claes R, et al. Validation of Computational Fluid Dynamics in CT-based Airway Models with SPECT/CT1. *Radiology* 2010; **257**(3). doi:10.1148/radiol.10100322/-/DC1.

22. Burrowes KS, De Backer J, Smallwood R, et al. Multi-scale computational models of the airways to unravel the pathophysiological mechanisms in asthma and chronic obstructive pulmonary disease (AirPROM). *Interface Focus* 2013; **3**(2). doi:10.1098/rsfs.2012.0057.

23. Burrowes KS, Doel T, Brightling C. Computational modeling of the obstructive lung diseases asthma and COPD. *Journal of Translational Medicine* 2014; **12**(Suppl 2):S5. doi:10.1186/1479-5876-12-S2-S5.

24. Qi S, Zhang B, Yue Y, et al. Airflow in Tracheobronchial Tree of Subjects with Tracheal Bronchus Simulated Using CT Image Based Models and CFD Method. *Journal of Medical Systems* 2018; **42**(4). doi:10.1007/s10916-017-0879-0.

25. Lin CL, Tawhai MH, McLennan G, Hoffman EA. Characteristics of the turbulent laryngeal jet and its effect on airflow in the human intra-thoracic airways. *Respiratory Physiology and Neurobiology* 2007; **157**(2–3):295–309. doi:10.1016/j.resp.2007.02.006.

26. Miyawaki S, Hoffman EA, Lin CL. Numerical simulations of aerosol delivery to the human lung with an idealized laryngeal model, image-based airway model, and automatic meshing algorithm. *Computers and Fluids* 2017; **148**:1–9. doi:10.1016/j.compfluid.2017.02.008.

27. Koullapis PG, Nicolaou L, Kassinos SC. In silico assessment of mouth-throat effects on regional deposition in the upper tracheobronchial airways. *Journal of Aerosol Science* 2018; **117**(December 2017):164–188. doi:10.1016/j.jaerosci.2017.12.001.

28. Verbanck S, Ghorbaniasl G, Biddiscombe MF, et al. Inhaled Aerosol Distribution in Human Airways: A Scintigraphy-Guided Study in a 3D Printed Model. *Journal of Aerosol Medicine and Pulmonary Drug Delivery* 2016; **29**:525–533. doi:10.1089/jamp.2016.1291.

29. Agnihotri V, Ghorbaniasl G, Verbanck S, Lacor C. On the multiple LES frozen field approach for the prediction of particle deposition in the human upper respiratory tract. *Journal of Aerosol Science* 2014; **68**:58–72. doi:10.1016/j.jaerosci.2013.11.001.

30. Yin Y, Choi J, Hoffman EA, Tawhai MH, Lin C-L. A multiscale MDCT image-based breathing lung model with time-varying regional ventilation. *Journal of computational physics* 2013; **244**:168–192.

31. Xia G, Tawhai MH, Hoffman EA, Lin C-L. Airway wall stiffening increases peak wall shear stress: a fluid-structure interaction study in rigid and compliant airways. *Annals of Biomedical Engineering* 2010; **38**(5):1836–1853. doi:10.1007/s10439-010-9956-y.

32. Park SJ, Kim JH, Kim KG, Lee SH. Intelligent measurement system of intrathoracic airways. In: *World Congress on Medical Physics and Biomedical Engineering 2006*. Springer Berlin Heidelberg; 2007:2544–2547.

33. Tu J, Inthavong K, Ahmadi. G. *Computational fluid and particle dynamics in the human respiratory system*. Springer Science & Business Media; 2012.

34. Versteeg HK, Malalasekera W. *An introduction to computational fluid dynamics: the finite volume method*. Pearson education; 2007.

35. Krause F, Wenk A, Lacor C, Kreyling WG, Möller W, Verbanck S. Numerical and experimental study on the deposition of nanoparticles in an extrathoracic oral airway model. *Journal of Aerosol Science* 2013; **57**:131–143. doi:10.1016/j.jaerosci.2012.11.004.

36. Atherton MA, Collins MW, Dayer MJ. *Repair and Redesign of Physiological Systems*. WIT Press;

2008.

37. Sul B, Wallqvist A, Morris MJ, Reifman J, Rakesh V. A computational study of the respiratory airflow characteristics in normal and obstructed human airways. *Computers in Biology and Medicine* 2014; **52**:130–143. doi:10.1016/j.compbiomed.2014.06.008.

38. Hyde DM, Hamid Q, Irvin CG. Anatomy, pathology, and physiology of the tracheobronchial tree: emphasis on the distal airways. *The Journal of allergy and clinical immunology* 2009; **124**(6 Suppl):S72–S77. doi:10.1016/j.jaci.2009.08.048.

39. Wu D, Miyawaki S, Tawhai MH, Hoffman EA, Lin CL. A Numerical Study of Water Loss Rate Distributions in MDCT-Based Human Airway Models. *Annals of Biomedical Engineering* 2015; **43**(11):2708–2721. doi:10.1007/s10439-015-1318-3.

40. Evans DJ, Green AS, Thomas NK. Wall shear stress distributions in a model of normal and constricted small airways. *Proceedings of the Institution of Mechanical Engineers, Part H: Journal of Engineering in Medicine* 2014; **228**(4):362–370. doi:10.1177/0954411914527586.

41. Ciofalo M, Di Liberto M. Transition to turbulence in serpentine pipes. *International Journal of Thermal Sciences* 2017; **116**:129–149. doi:10.1016/j.ijthermalsci.2017.02.010.

42. Thiriet M. *Anatomy and physiology of the circulatory and ventilatory systems*. Springer; 2014.

43. Boiselle PM, Lynch D (ed. . *CT of the Airways*. Springer Science & Business Media; 2008.

44. Miyawaki S, Choi S, Hoffman EA, et al. A 4DCT imaging-based breathing lung model with relativehysteresis. *Journal of computational physics* 2016; **326**:76–90. doi:10.1016/j.jcp.2016.08.039.A.

45. Lehmann M, Oehler B, Zuber J, et al. Redistribution of pulmonary ventilation after lung surgery detected with electrical impedance tomography. *Acta Anaesthesiologica Scandinavica* 2020; **64**(4):517–525. doi:10.1111/aas.13525.

46. LoMauro A, Aliverti A, Chiesa M, et al. Ribcage kinematics during exercise justifies thoracoscopic versus postero-lateral thoracotomy lobectomy prompt recovery. *European Journal of Cardio-thoracic*

Surgery 2017; **52**(6):1197–1205. doi:10.1093/ejcts/ezx174.

47. Shih TC, Hsiao H Da, Chen PY, Tu CY, Tseng TI, Ho YJ. Study of pre- and post-stent implantation in the trachea using computational fluid dynamics. *Journal of Medical and Biological Engineering* 2014; **34**(2):150–156. doi:10.5405/jmbe.1240.

48. Brouns M, Jayaraju ST, Lacor C, et al. Tracheal stenosis: A flow dynamics study. *Journal of Applied Physiology* 2007; **102**(3):1178–1184. doi:10.1152/japplphysiol.01063.2006.

49. Goodman L. Postoperative chest radiograph: II. Alterationsn after major intrathoracic surgery. *AJR American Journal of Roentgenology* 1980; **134**:803–813. doi:10.2214/ajr.134.4.803.

50. Kakeda S, Kamada K, Aoki T, Watanabe H, Nakata H. Postsurgical change in the tracheal bifurcation angle after upper lobectomy: radiographic evaluation. *Academic Radiology* 2003; **10**:644–649. doi:10.1016/s1076-6332(03)80083-1.

51. Larsen KS, Skoffer B, Gregersen Oestergaard L, Van Tulder M, Petersen AK. The effects of various respiratory physiotherapies after lung resection: a systematic review. *Physiotherapy Theory and Practice* 2020; **36**(11):1201–1219. doi:10.1080/09593985.2018.1564095.

52. Seok Y, Jheon S, Cho S. Serial changes in pulmonary function after video-assisted thoracic surgery lobectomy in lung cancer patients. *Thoracic and Cardiovascular Surgeon* 2014; **62**(2):133–139. doi:10.1055/s-0033-1343980.

53. Yin Y, Choi J, Hoffman EA, Tawhai MH, Lin C-L. Simulation of pulmonary air flow with a subject-specific boundary condition. *Journal of Biomechanics* 2010; **43**(11):2159–2163.

54. Qi S, Zhang B, Teng Y, et al. Transient Dynamics Simulation of Airflow in a CT-Scanned Human Airway Tree: More or Fewer Terminal Bronchi? *Computational and Mathematical Methods in Medicine* 2017; **2017**. doi:10.1155/2017/1969023.

55. Stylianou FS, Sznitman J, Kassinos SC. Direct numerical simulation of particle laden flow in a human airway bifurcation model. *International Journal of Heat and Fluid Flow* 2016; **61**:677–710. doi:10.1016/j.ijheatfluidflow.2016.07.013.

56. Tawhai MH, Hunter P, Tschirren J, Reinhardt J, McLennan G, Hoffman EA. CT-based geometry analysis and finite element models of the human and ovine bronchial tree. *Journal of Applied Physiology* 2004; **97**(6):2310–2321. doi:10.1152/japplphysiol.00520.2004.

57. Trabelsi O, del Palomar AP, López-villalobos JL, Ginel A, Doblaré M. Experimental characterization and constitutive modeling of the mechanical behavior of the human trachea. *Medical Engineering and Physics* 2010; **32**(1):76–82. doi:10.1016/j.medengphy.2009.10.010.

58. Zhu Z, Zhang C, Zhang L. Experimental and numerical investigation on inspiration and expiration flows in a three-generation human lung airway model at two flow rates. *Respiratory Physiology and Neurobiology* 2019; **262**(28):40–48. doi:10.1016/j.resp.2019.01.012.

59. Jayaraju ST, Brouns M, Lacor C, Belkassem B, Verbanck S. Large eddy and detached eddy simulations of fluid flow and particle deposition in a human mouth-throat. *Journal of Aerosol Science* 2008; **39**(10):862–875. doi:10.1016/j.jaerosci.2008.06.002.

TABLE 1: Acquisition parameters for preoperative and postoperative Computed Tomography (CT) images

Parameter	**CT Preoperative**	**CT Postoperative**
Contrast medium	No	Yes
Scanner	GE Medical System Optimact660	Siemens Somatom Definition
Slice thickness	0.625 mm	1.500 mm
Voxel size	0.7285×0.7285×0.6250 mm/voxel	0.8359×0.8359×1500 mm/voxel
Reconstruction kernel	B31f	B40f

TABLE 2: Fundamental dimensions of the laryngeal model. In the left column, the model parameters proposed by [26], as a function of the trachea hydraulic diameter, are stated. In the second and the third column, the dimensions of the reconstructed models for the preoperative and the postoperative geometry are reported, respectively

Model parameter	**Preoperative [cm]**	**Postoperative [cm]**
$D_{h,t}$	1.66	1.57
$D_{h,g} = 0.677\ D_{h,t}$	1.12	1.06
$D_{h,gu} = 1.24\ D_{h,t}$	2.06	1.95
$l_{gu} = 1.3\ D_{h,t}$	2.16	2.04
$l_{gl} = 1.3\ D_{h,t}$	2.16	2.04
$L_g = 8.64\ D_{h,t}$	14.34	13.56

TABLE 3: Preoperative and postoperative mesh refinements for the mesh independency analysis of the results

		Preoperative			**Postoperative**		
	Max bulk cell size	**N° cells**	**N° nodes**	**skewness**	**N° cells**	**N° nodes**	**skewness**
Mesh 1	1.5 mm	10.0×10^6	4.2×10^6	0.83	6.6×10^6	2.7×10^6	0.72
Mesh 2	1.3 mm	12.5×10^6	5.2×10^6	0.83	9.0×10^6	3.7×10^6	0.73
Mesh 3	1.2 mm	23.2×10^6	9.5×10^6	0.83	18.9×10^6	6.7×10^6	0.72

TABLE 4: Maximum values of the variables of interest for the preoperative and the postoperative geometries. The maximum velocity is found at the inlet of the trachea. The maximum wall pressure and wall shear stress are found at the Carina bifurcation. The percentage increment in the postoperative geometry is also reported

Maximum values	**Preoperative**	**Postoperative**	**Increment**
Velocity (m/s)	4.16	5.40	23 %
Inlet pressure (Pa)	16.42	31.08	47 %
Wall pressure (Pa)	11.87	22.96	48 %
Wall shear stress (Pa)	1.03	1.69	39 %

TABLE 5: Regional pressure drop for each lobe before and after surgery, calculated as the pressure difference between the pressure at an upstream section at the lobe entrance and the outlet pressure. The postoperative pressure shows an increment at the entrance of each lobe

Lobe	Preoperative pressure (Pa)	Postoperative pressure (Pa)	Increment
RUL	5.57	15.97	10.39
RML medial	4.5	13.55	8.76
RML lateral	4.9	13.66	9.05
RLL	4.57	13.41	8.84
LUL	6.02	-	-
LLL	6.28	16.36	10.08

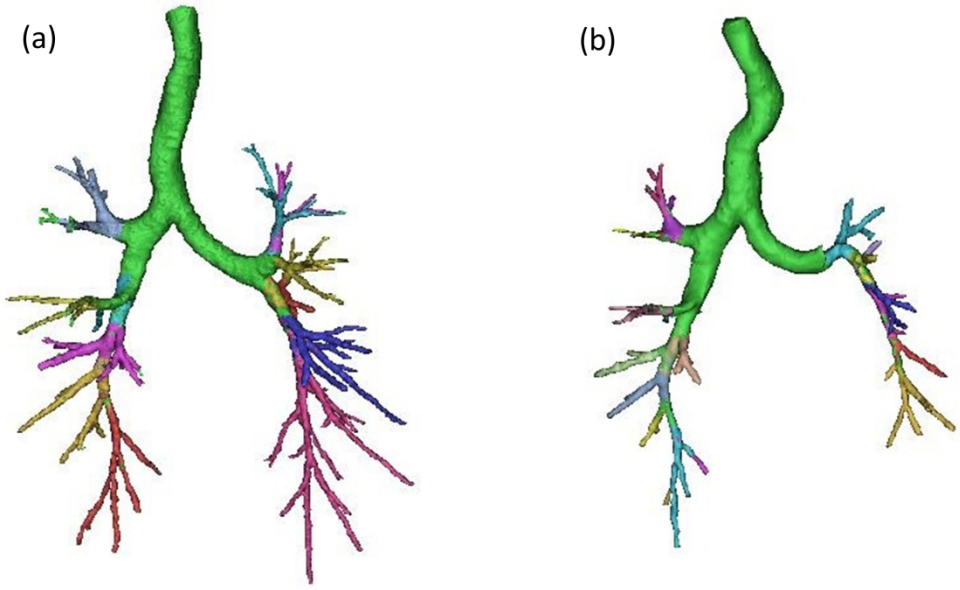

FIGURE 1 Geometry reconstruction from Computed Tomography (CT) images of the studied patient before (a) and after (b) surgery. The green part of the trachea and main bronchi is obtained through the automatic segmentation algorithm by Park et al. [30]; the different colored regions are obtained by manual segmentation process. The consequences of lobe resection and mediastinum shifting were recreated and consisted in the tracheal and bronchial bending, the presence of the suture zone, and the restriction of the left-lower bronchial lumen

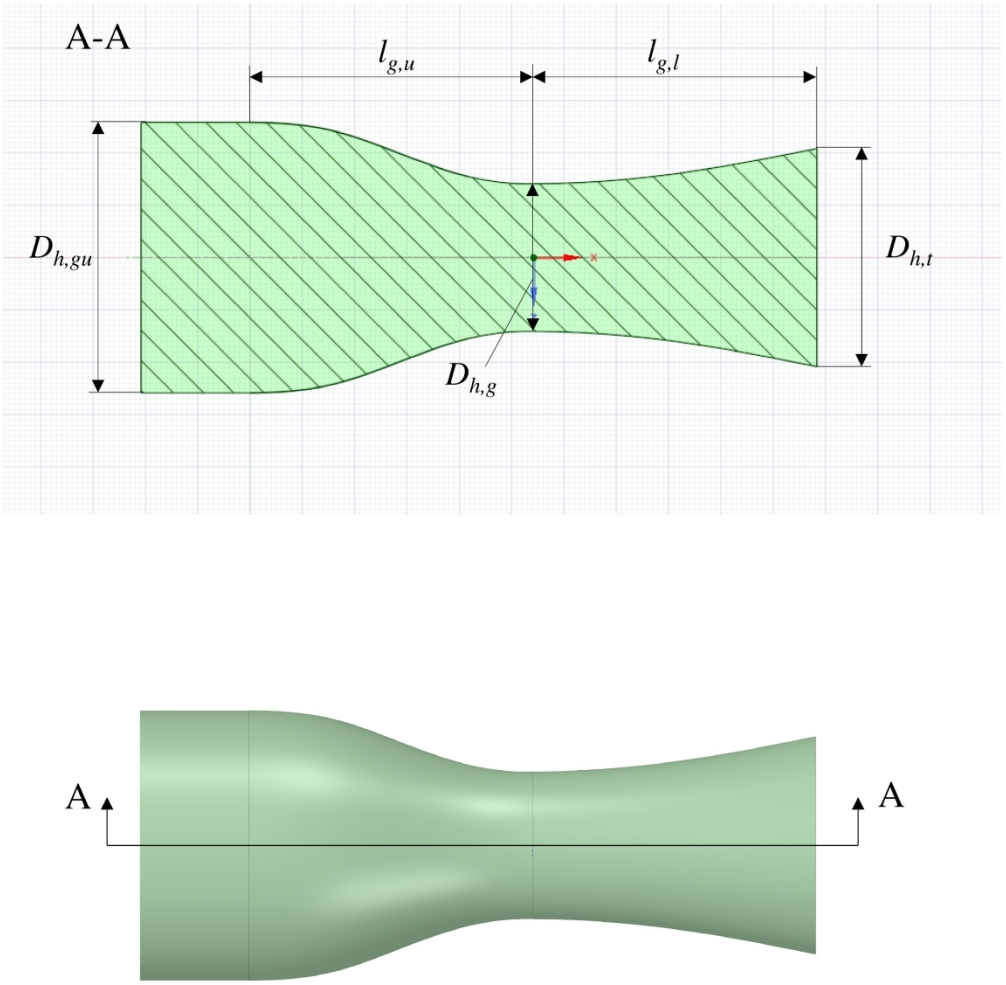

FIGURE 2 Reconstruction of the laryngeal model proposed by Miyawaki et al. [25]. In the section view at the top of the figure, the model parameters are defined: the hydraulic diameter of the trachea $D_{h,t}$; the hydraulic diameter at the glottis $D_{h,g}=0.677D_{h,t}$; the hydraulic diameter upstream the glottis $D_{h,gu}=1.24D_{h,t}$; the length of the larynx upstream the glottis $l_{gu}=1.3D_{h,t}$; and the length of the larynx downstream the glottis $l_{gl}=1.3D_{h,t}$. The resulting CAD model at the bottom of the figure was merged to the patient airway models

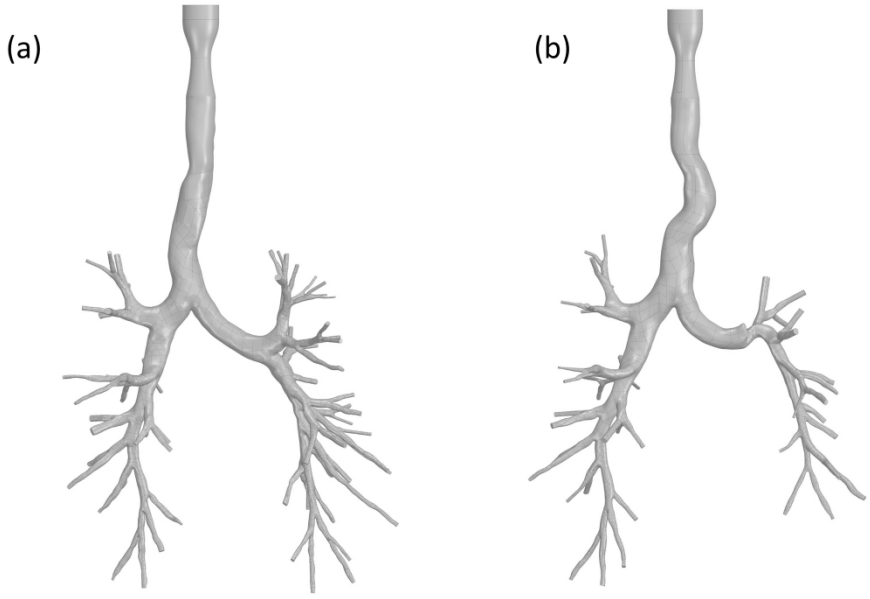

FIGURE 3 Geometrical CAD models for the preoperative case (a) and for the postoperative case (b). The tracheobronchial tree reconstructed from the CT images of the patient was merged with the laryngeal artificial model at the top part of the trachea

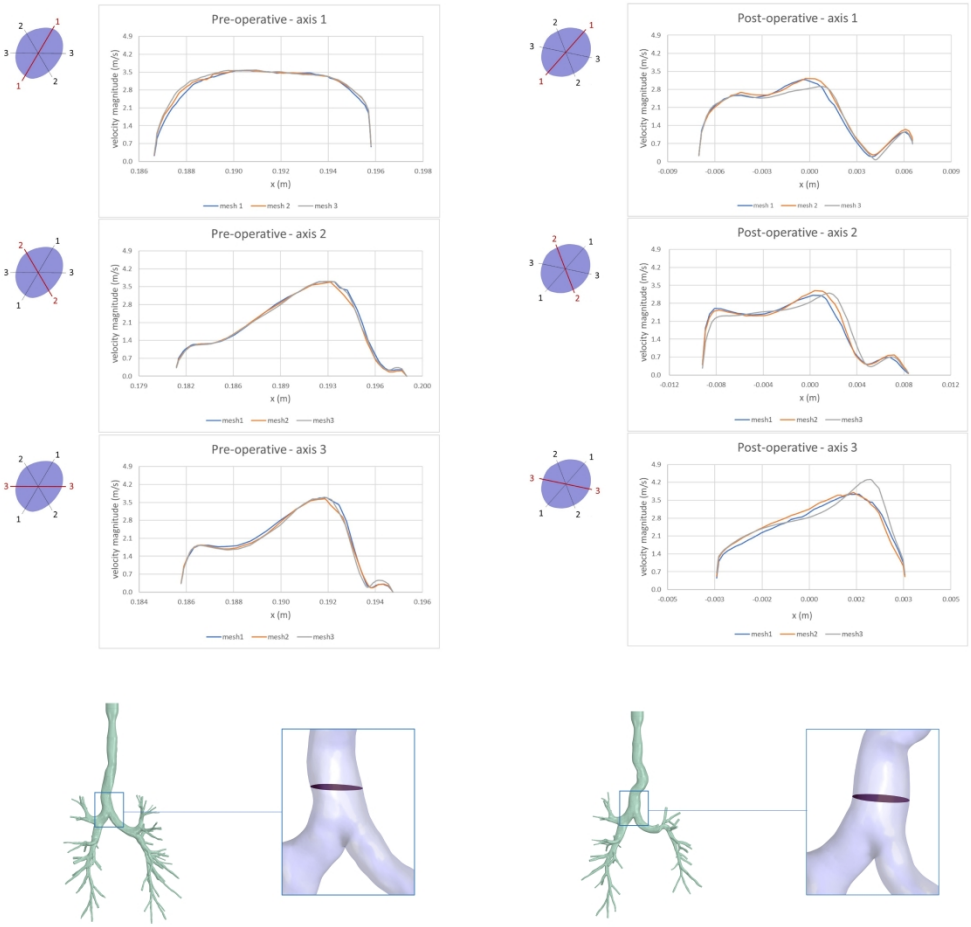

FIGURE 4 Mesh independence for preoperative configuration (on the left) and postoperative configuration (on the right). The velocity profiles were plotted along three axes (mutually rotated at 60 degrees from each other) located in a cross-sectional plane at 2 cm distance from the carina bifurcation. No significant differences were found among the profiles

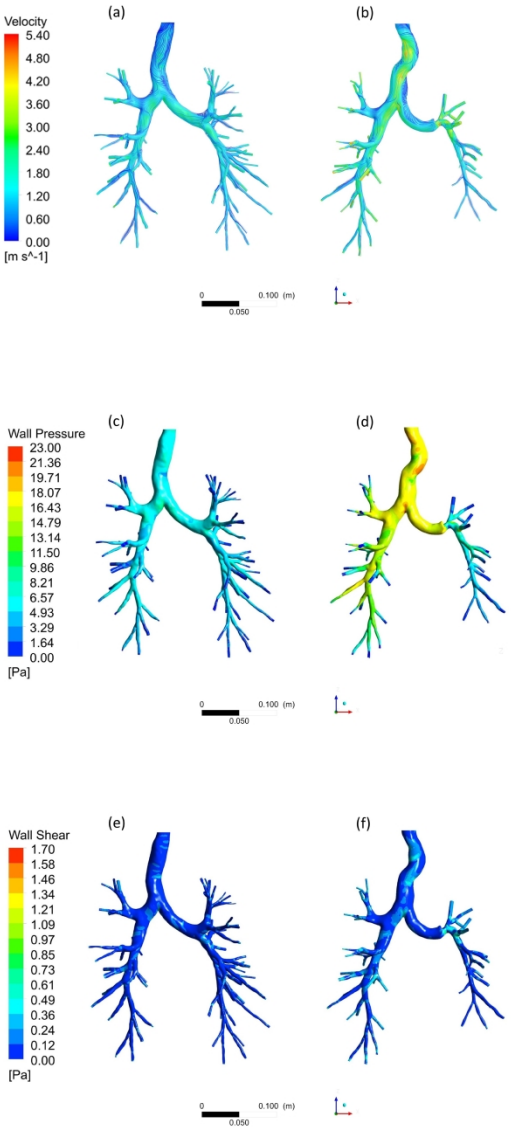

FIGURE 5 Overall fluid dynamics behavior in the preoperative and postoperative geometries. Comparing the two cases, the postoperative tree presented worsening air dynamic conditions, even on the right side, where no surgery was performed. The velocity streamlines (a, b) evidenced regions of higher air speed propagating from the trachea up to the smallest bronchi. The wall pressure (c, d) increased dramatically in the entire tree after surgery, with regions of peak values in the trachea and in the carina bifurcation. Regions of higher wall shear stress (e, f) were present in the trachea and in the left lower bronchus after lobectomy

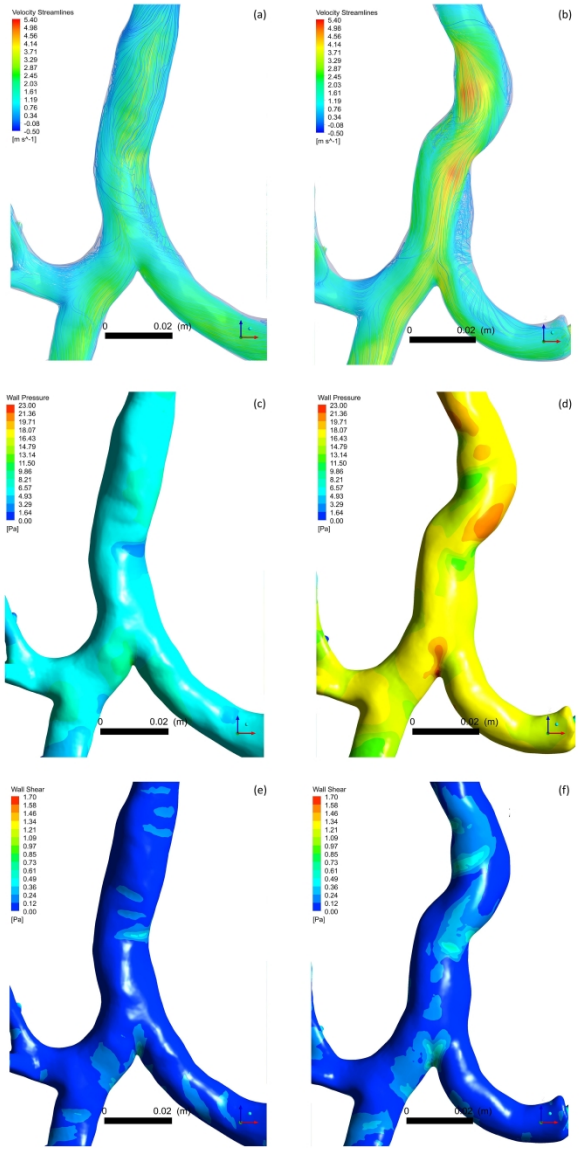

FIGURE 6 Fluid dynamics comparison of the preoperative and postoperative trachea. The parameters of velocity magnitude (a, b), wall pressure (c, d), and wall shear stress (e, f) are shown. The preoperative trachea presented smoother gradients of velocity, and more uniform pressure and wall shear stress values. After surgery, structural modifications due to mediastinum shifting and hemidiaphragm rising led to tracheal curvatures, with a completely different fluid dynamics: local velocity and pressure peaks occurred due to bending, and regions of higher wall shear stress expanded

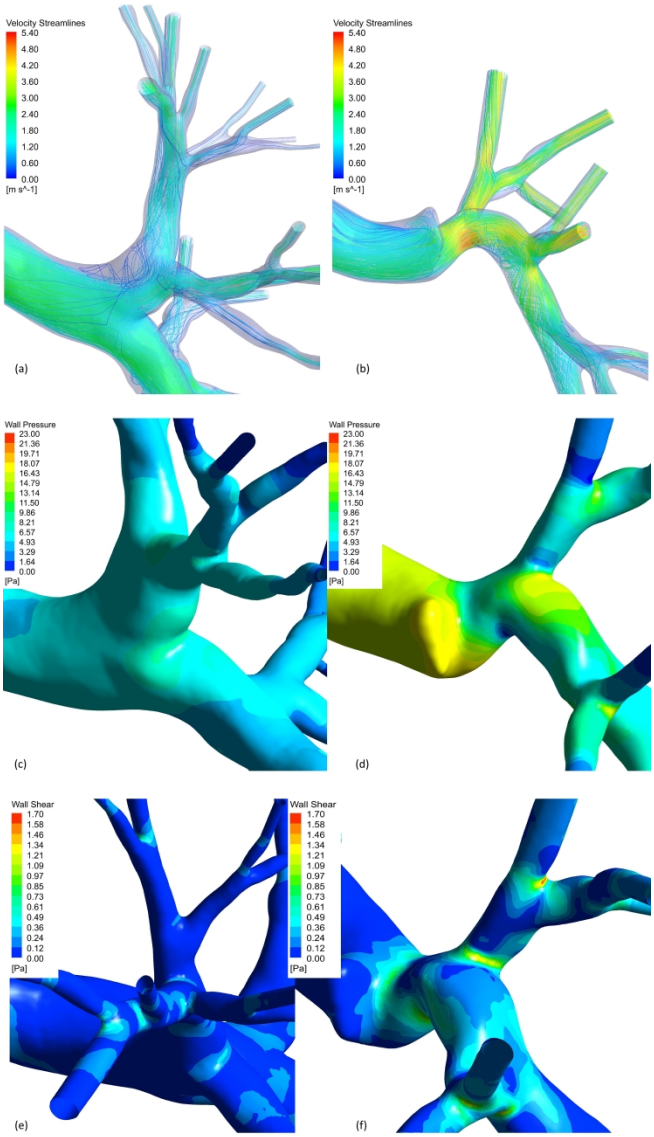

FIGURE 7 Zooming on the site of surgery: fluid dynamics comparison of left side of the tree. Velocity streamlines (a, b) show the abrupt change of air passage through the left lower bronchus after surgery, where a severe bending and a lumen restriction were found. In the suture zone and in the following bifurcations, a peak of pressure was found (c, d), and the wall shear stress contours (e, f) evidenced higher values at the bifurcations after surgery

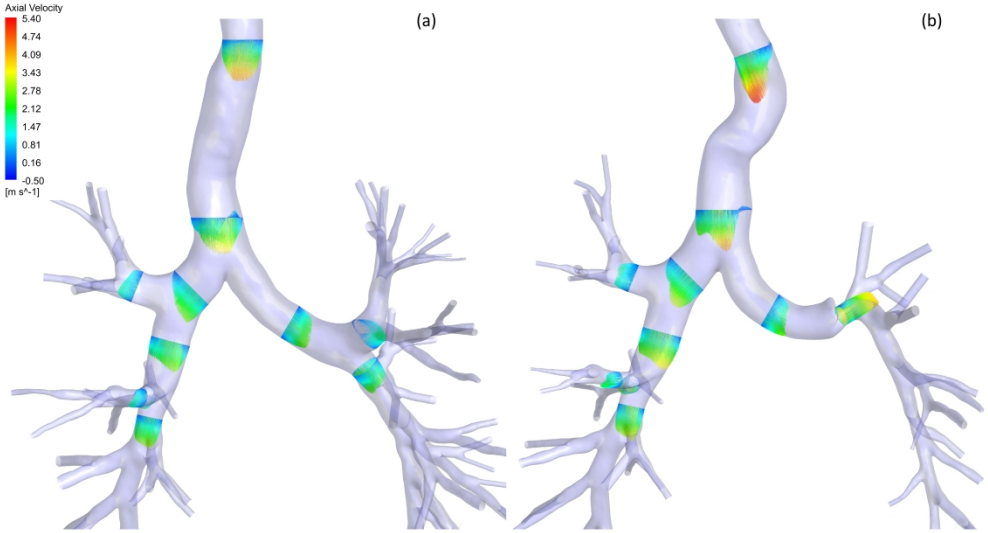

FIGURE 8 Plot of the axial velocity component, along the preferential direction of the flow in different cross-sectional planes, for the preoperative case (a) and for the postoperative case (b). A better visualization of the velocity at local level is given. At the trachea and at the left lower bronchus, the profile evidenced a worsening situation after surgery. In both geometries, reverse flow was revealed close to the carina bifurcation, and the maximum values along the following bronchi are shifted towards the inner side of the lumen, with greater values in all the postoperative planes

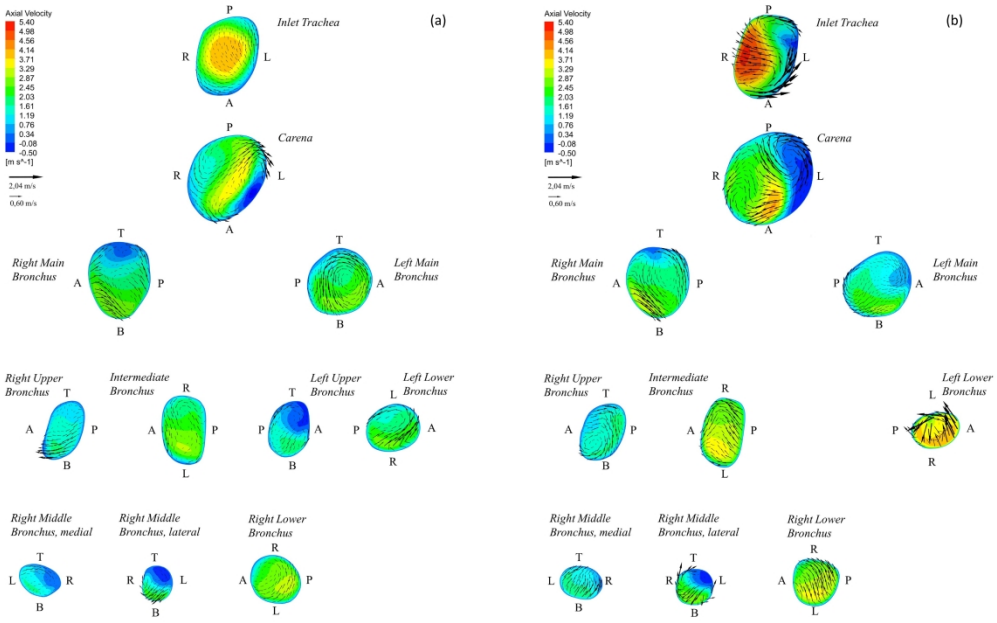

FIGURE 9 Axial velocity contours with the vectors of the in-plane velocity components (black arrows) for the preoperative (a) and postoperative (b) cases. Letters indicate the plate orientation inside the airway tree: posterior (P), anterior (A), right (R), left (L), top (T), bottom (B). The velocity can be observed in all its components and in relation to the cross-section. At the trachea, the in-plane velocity components intensified after lobectomy, determining a strongly different air transport in this zone. The situation in the right side of the tree is better discernible: the intermediate bronchus plate and its following branches presented increased values of velocity components. The left upper bronchus is missing, while the area restriction at the left lower bronchus entrance is remarkable, as the increments of velocity magnitude

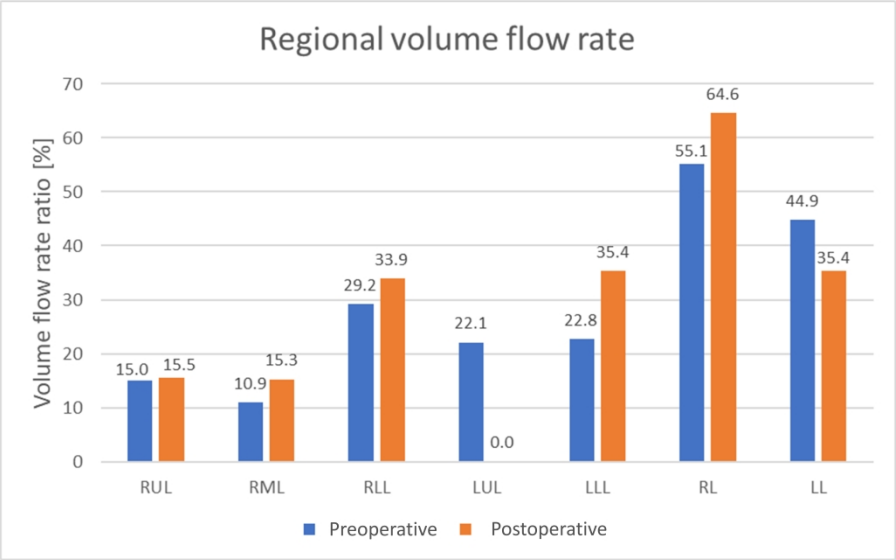

FIGURE 10 Regional Volume Flow Rate (VFR) in percentage values for the preoperative case (blue) and for the postoperative case (orange): right-upper lobe (RUL), right-middle lobe (RML), right-lower lobe (RLL), left-upper lobe (LUL), left-lower lobe (LLL), right lung (RL), and left lung (LL). In the preoperative case the ventilation of the right lung is greater with the respect to the left lung. This gap increased due to surgery. Locally, after surgery, the RUL ventilation was almost unchanged, while an increased VFR was present in RML and in the RLL. After lung resection, a null VFR occurred at the LUL, while a remarkable ventilation increment occurred at the LLL